

CNT@SrTiO₃ Nanocomposites Synthesized by In Situ Reaction for a High-Performance Flexible Supercapacitor

Yue Cao, Shijingmin Li, Jinhua Zhong, Yi Cao,* and Wenfeng Qiu*

Cite This: *ACS Omega* 2024, 9, 22423–22435

Read Online

ACCESS |



Metrics & More

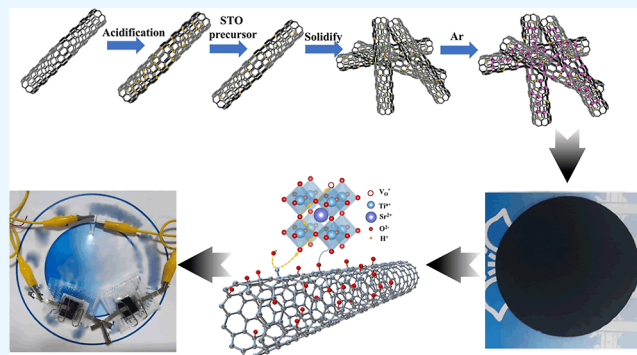


Article Recommendations



Supporting Information

ABSTRACT: This study presents the in situ synthesis of CNT@SrTiO₃ nanocomposite films for the development of high-performance flexible supercapacitors. The synthesis process involved the use of organic–inorganic hybrid polymers containing metal elements as precursors for thermal decomposition reaction under a reducing atmosphere. Due to the formation of chemical bonding between Ti elements and the CNTs, the interface between STO and CNT surface could provide additional active sites for ion transport and storage. Thereby, the incorporation of SrTiO₃ nanoparticles into CNTs enhanced the electrochemical performance of the resulting nanocomposite membranes. To further investigate the influence of STO content and synthesis temperature, we conducted a detailed analysis. The findings indicated that the CNT@STO film with 25% STO content, synthesized at 700 °C, and possessed optimal performance with an areal capacitance of 6682 mF·cm⁻² at 5 mV·s⁻¹. Furthermore, a symmetrical flexible supercapacitor assembled by two CNT@STO-25 electrodes demonstrated strong application potential in wearable devices, owing to its long cycle life, excellent flexibility, and high energy density of 430.2 μWh·cm⁻² (corresponding power density of 4.5 mW·cm⁻²). Based on these results, we believe that this study provides a fresh idea for the development of novel flexible energy storage materials.



1. INTRODUCTION

Nowadays, the development of renewable energy is directly related to progress in energy storage systems.¹ Among various potential energy storage and conversion devices, supercapacitors have driven significant interest to researchers owing to their superior power density, fast charge/discharge rate, and long cycle life.² Herein, in the last few decades, supercapacitors have been successfully utilized in many fields, including consumer electronics,³ military affairs,⁴ transport infrastructure,⁵ and electricity networks.⁶ In particular, on the wearable and portable electronic device side, flexible supercapacitors are favored by both academia and industry, which is attributed to their excellent stability and outstanding safety on the application.^{7,8} However, their disadvantage of low energy density still restricts their development.⁹ For meeting more possible applications, it is necessary to further address the defect.

In order to improve the energy density of supercapacitors, a lot of research has focused on their electrode materials.^{10–12} According to electrochemical theory, the specific capacitance and working voltage can both play significant roles in regulating the energy density. Thereby, the energy storage performance of flexible supercapacitor can be enhanced from these two aspects.¹³ Normally, carbon materials and their derivatives,^{14,15} such as carbon gel,¹⁶ carbon nanotubes (CNTs),¹⁷ and graphene,¹⁸ are considered as popular flexible

electrode materials due to their superior comprehensive mechanical properties and good capacitance performance.¹⁹ Previous studies suggest that it is appropriate to promote their specific capacitance or adjust voltage window through introducing oxygen- and nitrogen-containing functional groups on the surface of carbon materials or combining metallic oxide materials to fabricate hybrid electrodes.^{20–23} For example, Prakash and Manivannan synthesized a N,B codoped graphene oxide (NB-GO) to improve the electrochemical properties of GO. Owing to the distinctive B and N coupling significantly, this electrode possessed excellent specific capacitance (885 F·g⁻¹), outstanding rate capability (525 F·g⁻¹ at 10 A·g⁻¹), and good cycle stability (77.8%), which was retained for 10,000 continuous cycles.²⁴ Cheng's research group prepared a composite of NiCoO₂@CNT with a novel mesoporous grape-like structure by using a mild method, in which metal oxide (MO) nanoparticles were bonded to CNTs like vines tightly. Based on the synergistic effect, the corresponding

Received: March 9, 2024

Revised: April 24, 2024

Accepted: April 26, 2024

Published: May 7, 2024



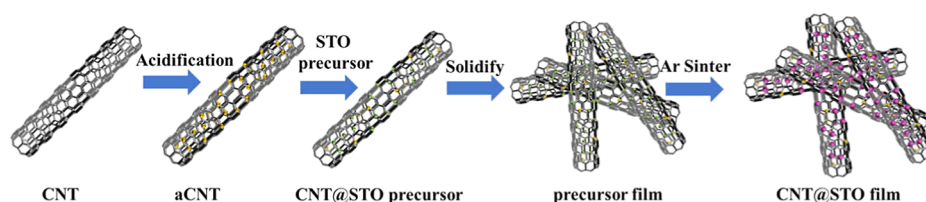


Figure 1. Preparation process of the CNT@STO composite film.

supercapacitor device exhibited a high energy density of 41.8 Wh kg^{-1} at 412 W kg^{-1} and an outstanding cycling property.²⁵ Jyothibas et al. prepared the cellulose/functionalized carbon nanotube (f-CNT)/ Fe_2O_3 (CCF) composite films through a simple, cost-effective, and environmentally friendly method. This film was used as freestanding negative electrodes in supercapacitors and exhibited outstanding areal ($9107.1 \text{ mF}\cdot\text{cm}^{-2}$) capacitance.²⁶ Although superior enhancement of specific capacitance benefits from these surface modifications, these reports still suffer from low working voltages due to their high dependence on surface faradaic redox reaction.

Nevertheless, a perovskite-type manganese oxides LaMnO_3 with an ABO_3 structure has been discovered and demonstrated as a novel energy storage material by the Mefford's group.²⁷ Based on the oxygen intercalation mechanism, in the charge/discharge process, the anion vacancies of oxides, including interstitial positions between lattice and oxygen defects in the lattice, can serve as charge storage sites.²⁸ As the pseudocapacitance derives from reversible insertion and deinsertion of OH^- ions, this oxide electrode can provide significantly broader potential windows of 1.8 V. In addition, numerous binary composite oxides possessing a similar perovskite structure, such as $\text{Sr}_2\text{CoMo}_{1-x}\text{Ni}_x\text{O}_{6-\delta}$,²⁹ BaMnO_3 ,³⁰ $\text{SrFe}_{1-x}\text{Zr}_x\text{O}_{3-\delta}$,³¹ and so on,³² also show high electrochemical performance according to this mechanism.³³ As a result, these kinds of oxides can reinforce the energy storage performance of carbon materials and maintain high conductivity through combining with them.^{34–36} Oliva et al.³⁷ added $\text{Ca}_{2.9}\text{La}_{0.1}\text{Co}_4\text{O}_9$ (CaLaCo) particles with a microplate morphology into the graphene electrode to improve the capacitance. Ultimately, the capacitive performance was enhanced by approximately 70%, while the charge-transfer resistance (R_{ct}) decreased by 80%. Undavalli Venkata Gopi's study indicated that LaNiO_3 could facilitate the rGO- LaNiO_3 composite to achieve faster electron transfer rates, which led to a high specific capacitance than that of rGO electrode.³⁸ Thus, it is desirable to combine flexible carbon materials with MOs following the oxygen intercalation mechanism to integrate their potentials.

CNT has achieved considerable attention from scientist and opened up a broad range of applications in supercapacitor field due to its excellent conductivity property, extended mechanical flexibility, and better structural stability.³⁹ In recent years, the design and study of inorganic hybrid carbon-based flexible energy storage materials, generally consisting of MOs and CNTs, have been developed extensively and quickly.^{40,41} The incorporation of MOs into CNTs not only addresses the challenges associated with low operating voltage and limited energy density in flexible supercapacitors but also enhances their application versatility in wearable devices due to their outstanding rate capability. Li et al. proposed an electrostatic self-assembly strategy for fabricating perovskite-type FeMnO_3 microspheres anchored within the CNT conductive network

(FeMnO_3 -CNTCN) as the anode materials for lithium-ion supercapacitor.⁴² Despite the splendid cyclability and superior energy density exhibited by this composite electrode, which benefit from the synergistic interplay between two components, the rate performance of the devices still needs improvement due to the relatively weak electrostatic interactions between the two components. However, our research group has confirmed that nano-MOs, such as $\text{Hf}_6\text{Ta}_2\text{O}_{17}$, prepared in situ on the surface of CNTs could effectively enhance electron and proton conduction, improve the access of active sites, and produce extra pseudocapacitance in the composite electrode.⁴³ Consequently, a novel appropriate oxide is in demand to modify the flexible CNT. Among various MOs, SrTiO_3 (STO) has been considered as one of the most attractive electrode materials not only because of its superior electrochemical property but also benefiting from the advantages of low cost, natural abundance, environmental safety, and low toxicity.

In this work, we synthesized the CNT@SrTiO_3 binary nanocomposite film as an efficient electrode for the flexible supercapacitor application. The nano-STO directly grew on the surface of CNT via covalent or noncovalent interaction and formed a grape-like structure. Meanwhile, the nanocomposite film could retain its excellent mechanical flexibility after the mild thermal treatment under an argon atmosphere. Because the shape, size, and interaction of STO all play an important role in electrochemical performance of composite, we investigated these factors impacted by changes in calcination temperature and STO concentration carefully. In addition, the electrochemical properties of the CNT@STO and the corresponding supercapacitor device were also studied in detail to demonstrate whether such nanocomposite materials were a good candidate for the application.

2. EXPERIMENTAL SECTION

2.1. Surface Modification of CNT. In this study, the CNTs (NTP8012, diameter: $<3 \text{ nm}$, purity: $>85.0 \text{ wt } \%$) were provided by Shen Zhen Nanotech Port Co., Ltd. To produce more active functional groups on the surface of CNTs, we treated them using a mixed acid of sulfuric acid and nitric acid (1:3 in volume). The process included adding CNTs into the mixed acid prepared before in the proportion of 1:150, heating to $70 \text{ }^\circ\text{C}$, agitating for 30 min, then washing them with deionized water and anhydrous ethanol, and finally obtaining surface-modified CNTs by vacuum drying at $40 \text{ }^\circ\text{C}$ for 24 h. Moreover, we denoted this product as a-CNT.

2.2. Preparation of the CNT@STO Composite Film. Herein, the preparation process is schematically shown in Figure 1. The STO precursors were prepared with isopropyl titanate ($\text{Ti}(\text{OPr}^i)_4$), strontium acetate ($\text{C}_4\text{H}_6\text{O}_4\text{Sr}$), and acetylacetone (Acac) as a primary substance for the controlled hydrolysis reaction and catalyzed by a weak base. First, $\text{Ti}(\text{OPr}^i)_4$, $\text{C}_4\text{H}_6\text{O}_4\text{Sr}$, and Acac were dissolved into n-

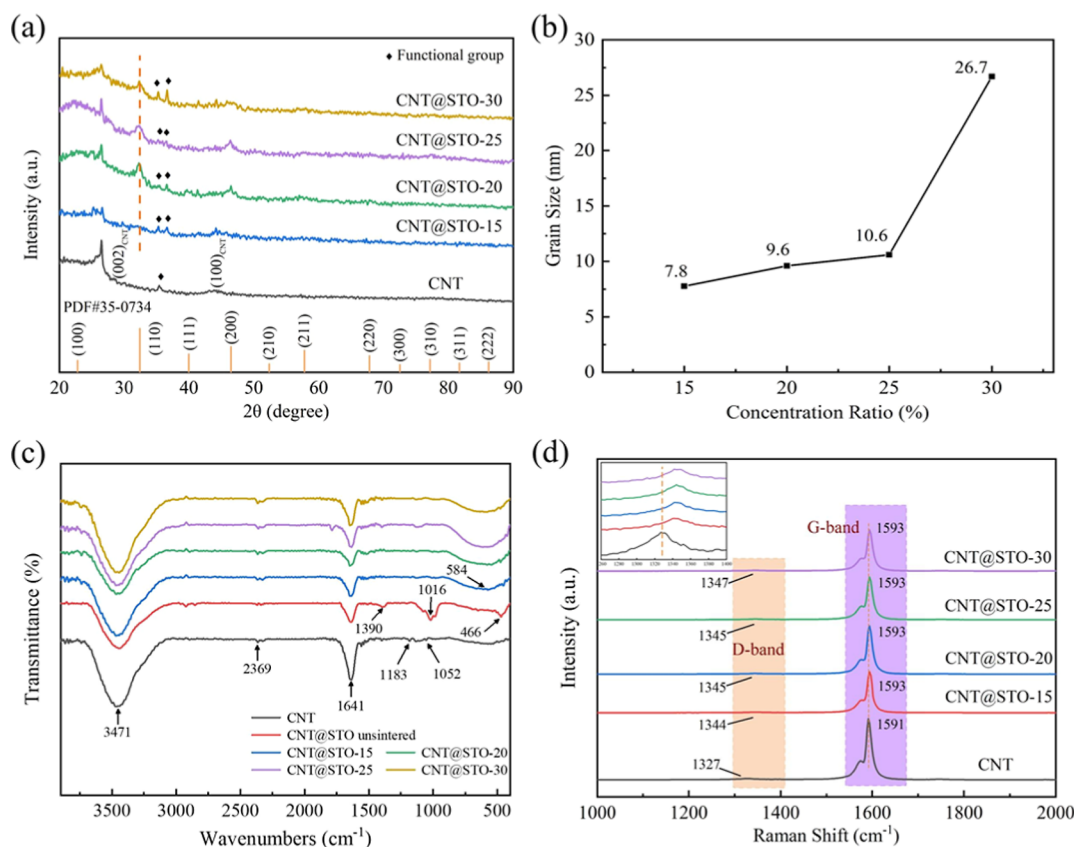


Figure 2. Characterization of CNT films and CNT@STO composite membrane: (a) XRD patterns, (b) average grain sizes, and (c) FTIR spectra. (d) Raman spectra.

propanol in a mole ratio of 1:1:0.9 to form a homogeneous mixture, recorded as solution A. Afterward, solution A was mixed with the a-CNT and heated to 90 °C with continuous stirring. Then, we added deionized water and 5% ammonia solution in succession, and the mixture was agitated and refluxed at 105 °C for 2 h. Finally, the cooled mixture formed a CNT@STO-precursor film by vacuum filtration. In this process, to give the product, n-propyl alcohol and deionized water were employed to wash the film 3 times repeatedly, in turn, for removing the organic solvents. After that, for the formation of crystalline STO and obtaining the CNT@STO film, the composite film was calcined under an Ar atmosphere for 2 h. In order to protect its integrity, we treated the composite film in a temperature range of 500–800 °C, which was below the temperature of carbon composition ablation. In addition, a CNT film that served as the control group was synthesized under the same treatment process.

2.3. Material Characterization. The morphology, elemental composition, and distribution of the samples were directly characterized with SEM (JEOL JSM-7900F), TEM (JEOL JEM-F200), and EDS (Bruker EDS QUANTAX). The lattice structures of composite were registered using an X'Pert PRC diffractometer (Netherlands, PANalytical) with Cu K α radiation at a scanning rate of 5° min⁻¹ ($\lambda = 0.15418$ nm). The distribution and valence state situation of various elements on the film surface were analyzed via X-ray photoelectron spectroscopy (XPS, ThermoFisher ESCALAB XI+). Electron paramagnetic resonance (EPR) measurement was carried out on a Bruker ELEXSYS-II E500 spectrometer. The Raman spectra of the samples were tested by a HJY LabRAM Aramis

spectrometer with a laser diode at an excitation wavelength of 532 nm.

2.4. Electrochemical Measurements. In general, the working electrodes were composed of current collector, adhesive, and active materials. In this study, various CNT@STO composite membranes and a CNT film were regarded as active materials. In addition, a mixture formed by dispersing conductive carbon black and poly(vinylidene fluoride) with a mass ratio of 1:1 in *N*-methyl pyrrolidone was used as the adhesive, while carbon paper cloth (Toray Industries, Inc., Japan) was applied as the collector. The working electrodes were assembled by adhering the active materials to the surface of the carbon cloth and drying them at 80 °C for 1 h. The area of these electrodes were in the range of 0.25 cm⁻².

To validate the practicality of the CNT@STO composite, a symmetrical supercapacitor device was fabricated using a pair of identical electrodes arranged in a sandwich structure, with 1 M Na₂SO₄ solution as the electrolyte. Moreover, both electrodes were connected to nickel tabs and separated by an organic ionic septum.

The electrochemical measurements of various working electrodes were conducted using a CHI760E workstation (Shanghai Chenhua, China) and employing a three-electrode system in a 1 M Na₂SO₄ electrolyte solution. A platinum wire and a saturated calomel electrode (SCE) were applied as the counter electrode and reference electrode, respectively. In addition, the flexible device was tested by using a two-electrode system, while one electrode was used as the working electrode and the other was used as the counter electrode and reference electrode. The areal capacitance (C_s , F·cm⁻²) was calculated

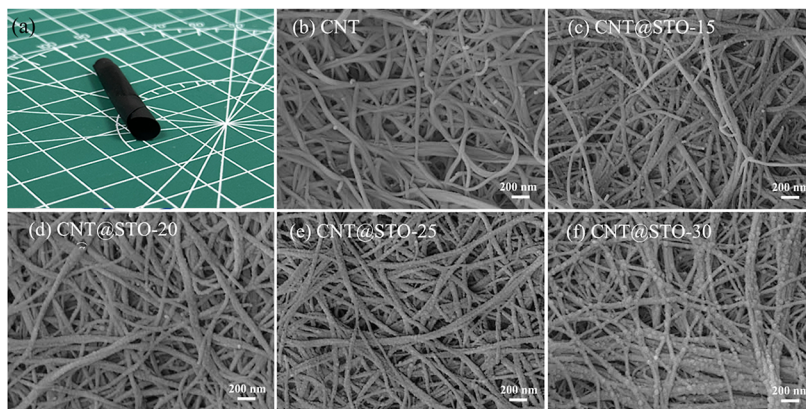


Figure 3. (a) Photograph of CNT and SEM images of (b) CNT, (c) CNT@STO-15, (d) CNT@STO-20, (e) CNT@STO-25, and (f) CNT@STO-30.

from the GCD curves or CV curves according to the following eq (eq 1)

$$C_s = I\Delta t / (S\Delta V) = Q / (2Sv\Delta V) \quad (1)$$

In eq 1, I (A) is the impressed current, Δt (s) is the discharge time, S (cm^2) is the area of the materials on each working electrode, and ΔV (V) is the voltage range of each scan. While Q is the integrated area of CV curve, v is the scanning rate, S (cm^2) is still the area of the materials on each working electrode, and ΔV (V) indicates the voltage range amplitude.

The energy density (E , Wh cm^{-2}) and power density (P , W cm^{-2}) of the symmetrical device were calculated by eqs 2 and 3, respectively

$$E = C_s V^2 / 7.2 \quad (2)$$

$$P = 3600E / t \quad (3)$$

3. RESULTS AND DISCUSSION

3.1. Influence of STO Ratio. In this study, the storage efficiency of the composite film impacted by the content of STO nanoparticles were investigated by various characterization methods carefully. Herein, we prepared four different groups of CNT@STO film, while the STO and CNT were combined at the mass ratios of 15:85, 20:80, 25:75, and 30:70, respectively. To ensure the formation of perovskite structure for the STO nanoparticles, all films were synthesized at 800°C under an Ar atmosphere. These four samples were denoted as CNT@STO-15, CNT@STO-20, CNT@STO-25, and CNT@STO-30, respectively. In addition, the mass ratio between the two is determined by TG and the results are plotted and displayed in Figure S1. According to the figures, the actual quality of STO is calculated and shown in Table S1. These findings suggested that these different composite membranes were all in good agreement with their original design.

Furthermore, their crystal structures are characterized by XRD patterns in a 2θ range of 20 to 90° and are exhibited in Figure 2a. From the drawing, the diffraction peaks at 26.4 and 43° have been proved as a characteristic peak belonging to the (002) and (100) planes of CNT. Furthermore, it is confirmed that small peaks nearby 35° can be attributed to the functional groups introduced by acidification treatment.⁴³ Owing to the presence of CNT peaks in every CNT@STO sample, we can identify that SWCNT is still maintaining its initial structure after calcination. Moreover, based on the standard card (PDF

#35–0734), various CNT@STO films all possess the main characteristic peak corresponding to the (110) plane of perovskite-type SrTiO_3 , which demonstrate the in situ generation of STO nanoparticles on the surface of CNTs. When the STO content increases, the intensity of (110) diffraction peak is also gradually enhanced, indicating better crystallinity. In addition, the fine stray peaks at $2\theta = 37^\circ$ observed in different CNT@STO may correspond to characteristic peaks of new functional groups, such as the Ti–O–C group formed in the heat treatment process, while the diffraction peaks around 35° may belong to the carboxyl groups on the CNT surface. Therefore, this finding can also determine the presence of strong chemical bonding rather than just weak Coulombic interactions between the in situ-grown STO and the surface of CNTs. As shown in Figure 2b, the average grain sizes of STO nanoparticles also grow up significantly with the increase of oxide ratio according to Scherrer's formula. In practice, not only the impurities in STO but also its enlarged particle size may both induce a low ion diffusion coefficient, which results in a reduction in energy storage capacity. Consequently, for higher electrochemical performance, an appropriate content of STO should be explored in detail.

In the case of CNT films remaining structurally intact after calcination, to investigate differences before and after sintering, the FTIR and Raman spectra were used for detecting micro changes in these films. The results are plotted in Figure 2c,d, respectively. From the analysis of the IR spectrum, it can be found that the absorption peaks attributed to the stretching vibration of C–H, C=C, and C=O for carboxyl functional groups appear at the same position in different samples with the wavelengths of 3471 , 2369 , and 1641 cm^{-1} , respectively. However, comparison with the CNT film, the intensity of corresponding peaks in CNT@STO-precursors and CNT@STO samples becomes weaker, due to the formation of chemical bonds between the organic groups on the surface of CNTs with the STO precursors or STO nanoparticles. In addition, the peaks at 1183 and 1052 cm^{-1} , belonging to the in-plane and out-of-plane vibrations of the –OH, disappear after compounding of CNT with STO precursors or oxides, which also give similar results. Moreover, a new peak observed at 1016 cm^{-1} can be attributed to the Ti–O–C=O bonds prepared by esterification between the carboxyl group on the CNT surface and titanate. Meanwhile, in the CNT@STO-precursor and four CNT@STO samples, the characteristic

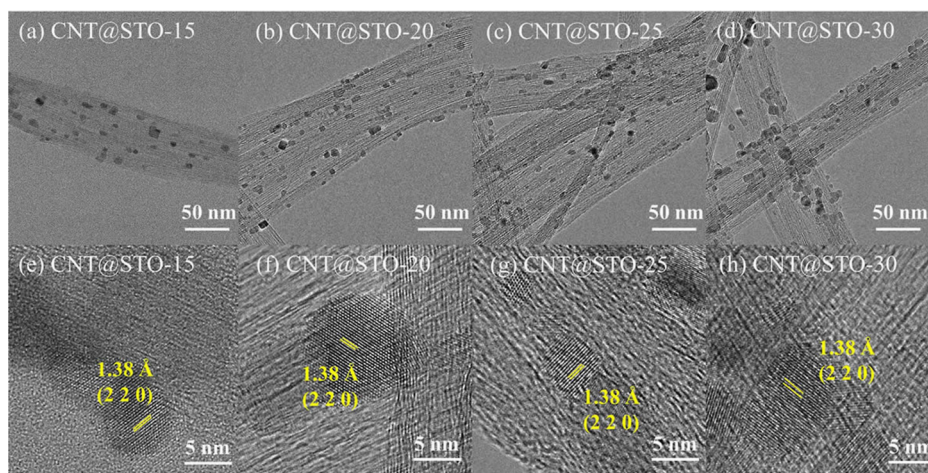


Figure 4. TEM images of (a) CNT@STO-15, (b) CNT@STO-20, (c) CNT@STO-25, and (d) CNT@STO-30 and HRTEM images of (e) CNT@STO-15, (f) CNT@STO-20, (g) CNT@STO-25, and (h) CNT@STO-30.

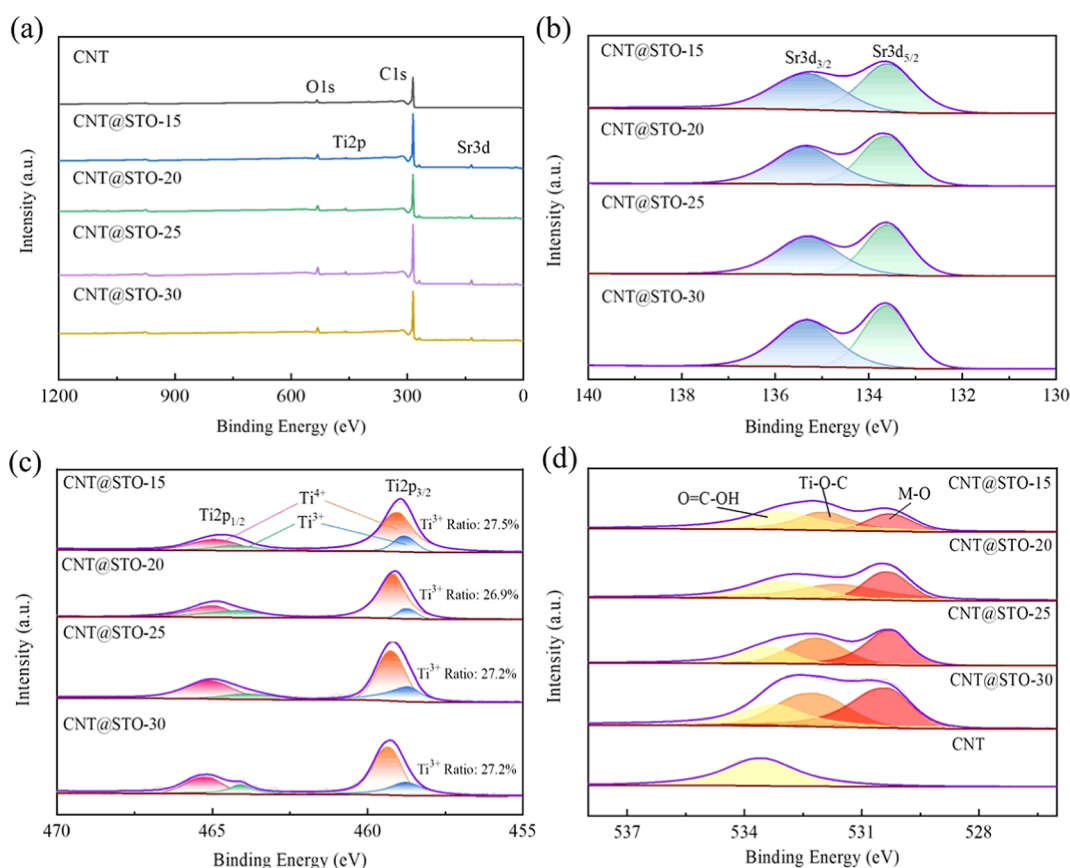


Figure 5. XPS spectra of CNT films and CNT@STO composite membrane: (a) full spectrum. (b) Sr 3d spectrum. (c) Ti 2p spectrum. (d) O 1s spectrum.

peaks representing metal–O bonds can be observed ranging from 400 to 800 cm^{-1} . With the increasing concentration of STO, the intensity of diffraction peak is enhanced significantly.

In order to further study the interface interaction between the STO nanoparticles and CNT, we analyze the Raman spectral data of various films in detail. As the D band in the CNT is generated by the defects, the G band comes from the vibration of sp^2 hybrid carbon atoms, the minor peaks of D band presented in all five samples suggest that CNTs in these films both possess a complete graphite structure. Nevertheless,

the I_D/I_G values (shown in Table S2) of the four CNT@STO samples have fallen, if modestly, indicating that the STO crystals prepared by the precursor method can react with carboxyl groups on the CNT surface and form strong interfacial interactions during the sintering process. Besides, compared to the CNT film, a red shift occurs in both G and D bands of the four CNT@STO films, also demonstrating the strong interfacial interaction between the STO crystal and CNT. This result can be attributed to M–O–C chemical bonds generated during thermal treatment. Owing to the Ti–

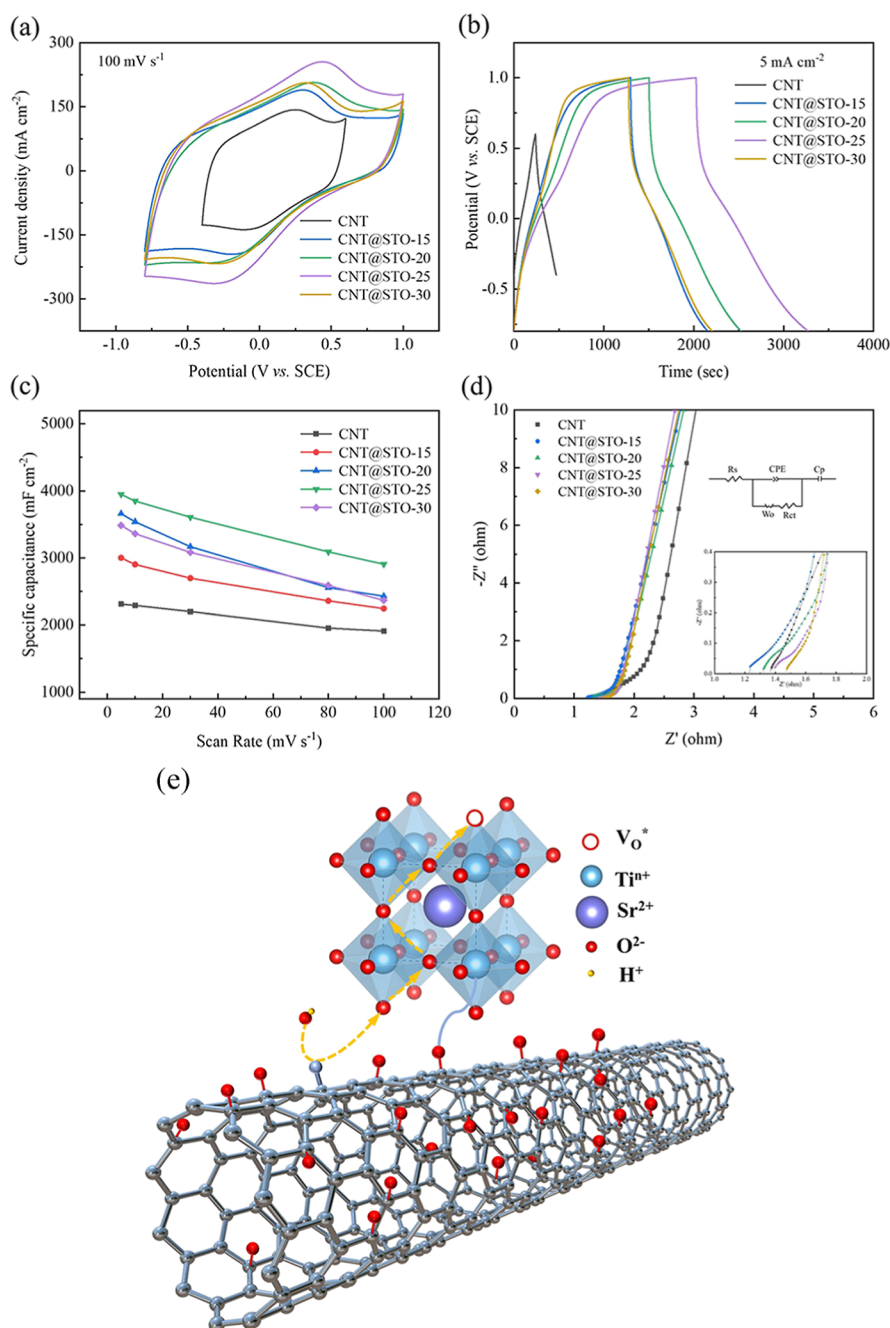


Figure 6. (a) CV curves of the CNT and various CNT@STO electrodes at 100 mV s^{-1} . (b) GCD curves of the CNT and various CNT@STO electrodes at 5 mA cm^{-2} . (c) Areal capacitance of different CNT@STO and standard CNT at different scan rates. (d) Nyquist plots of different CNT@STO and standard CNT electrodes in $1 \text{ M Na}_2\text{SO}_4$. The inset is the equivalent circuit diagram, (e) mechanism of oxygen intercalation into CNT@STO- x .

O=C=O bonds produced by the reaction of $-\text{COOH}$ and Ti-OR bonds, the STO precursor is firmly bound to acid-modified CNT. Whereas, sintering under a reducing atmosphere promotes the Ti-O-C=O bonds to decompose and carbonize, eventually form the Ti-O-C bonds and reduce the defects of CNT. In conclusion, based on the previous study, we can deduce that this interaction may drastically improve the charge storage performance of CNT@STO.

Meanwhile, the microcosmic appearance of various CNT@STO films was analyzed by using SEM, and the results are displayed in Figure 3. These images show that all CNTs in

these different CNT@STO samples can maintain their integral nanotube structure after sintering. In this work, the vine-like CNT crisscross and overlap to provide a flexible film, while the STO nanoparticles are bonded to the surface of CNTs and form a novel grape-like structure. Moreover, with the increase of STO content, its particle size gradually increases, and the surface of CNTs progressively turns more rougher. Especially in the CNT@STO-30 sample, the particle size of STO is close to the diameter of CNT, which may impact the adsorption and transport of anions.

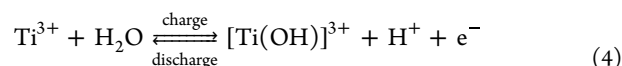
Additionally, the morphology and microstructure of these composite membranes were observed and analyzed using TEM

and HRTEM, respectively. As shown in Figure 4, for these films, the STO particles with different amounts and sizes can be both adhered tightly to the CNT surface. And the variation pattern of particle size is also consistent with the above results. In these HRTEM images, the lattice stripes of perovskite-type STO, belonging to the (220) plane, are clearly visible in every CNT@STO sample, and the interplanar spacing remains constant at 1.38 Å. However, the STO nanoparticles in the CNT@STO-30 present a much larger grain size and undergo severe aggregation on the surface of CNT, which may lead to its degradation of performance. In general, the microstructure of CNT is retained after annealing, while the STO can also obtain a complete lattice simultaneously, but the STO content still needs to be elaborately designed.

To verify the formation of STO nanoparticles and study the interaction principle between the surface of CNT and STO, we performed the XPS measurement to characterize CNT film and four CNT@STO samples. Figure 5a displays the corresponding characteristic peaks of Sr, Ti, O, and C in different CNT@STO samples, confirming the existence of STO and CNT. In addition, as shown in Figure 5b,c, the intensity of the Sr 3d and Ti 2p peaks has grown with the increase of the STO ratio obviously. Besides, the Ti 2p_{3/2} and Ti 2p_{1/2} spin-orbit peaks can be both divided into two split peaks after software fitting, belonging to characteristic peaks of Ti³⁺ and Ti⁴⁺, respectively. According to the fitting results, the proportions of Ti³⁺ in these CNT@STO samples are consistently maintained at about 27%. This may be attributed to sintering in a reducing atmosphere, which results in the partial reduction of Ti⁴⁺ to trivalence and the generation of numerous oxygen defects on the STO surface. Based on our previous reports, these defects can not only enhance the adsorption and transport efficiency of anions but also serve as charge storage sites. Simultaneously, in this study, the active groups on the CNT surface after acidification can bond with these surface oxygen defects of STO and form stable M–O–C chemical bonds during the heat treatment process. The O 1s XPS spectrum of CNT@STO and CNT films would further confirm that the interaction is induced by the M–O–C bonds. In Figure 5d, the peaks of the O 1s of CNT@STO-15, CNT@STO-20, CNT@STO-25, and CNT@STO-30 all consist of two adjacent spin-orbit peaks at binding energies of 532.5 and 530.3 eV, corresponding to C–O bonds and M–O bonds at the interface, respectively. However, the CNT exhibits only one O 1s peak representing C–O bonds at 533.5 eV. Therefore, the two split peaks divided from O 1s peaks at 532.5 eV, which are attributed to different types of C–O bonds, including carboxyl groups on the CNT surface and M–O–C bonds, respectively. Meanwhile, the peaks of M–O bonds represent the oxygen species in STO. As the STO content increases, the ratio of oxygen species corresponding to carboxyl groups drops rapidly owing to consumption through thermal decomposition. However, the proportions of M–O–C are increased. These results all suggest that M–O–C bonds, rather than weak intermolecular interactions, provide the strong bonding interface and endow the CNT@STO with unique properties.

The electrochemical properties of different CNT@STO films affected by the factors of interface interaction and STO ratios were investigated in detail by cyclic voltammetry (CV) and galvanostatic charge–discharge (GCD) tests in the 1 M Na₂SO₄ solution. The various CV and GCD curves corresponding to CNT, CNT@STO-15, CNT@STO-20, CNT@STO-25, and CNT@STO-30 are presented in Figure

S2 and S3. For the purpose of contrast analysis, we show the CV curves of these different electrodes obtained at the same scan rate of 100 mV·s⁻¹ in Figure 6a. Unlike the rectangular curve of conventional double layer capacitors (DLCs), all CNT@STO films possess a deformed rectangle shape with a couple of broad peaks, which can be attributed to the reversible redox reaction of the interconversion between Ti³⁺/Ti⁴⁺. Furthermore, these CNT@STO electrodes exhibit a wider voltage window of 1.8 V than CNT's 1 V. This indicates that CNT films modified by STO nanoparticles perform obvious pseudocapacitance characteristics, and the corresponding Faraday reaction can be described by the following equation



Moreover, different from the mirror-symmetric GCD curve of CNT, Figure 6b presents various similar asymmetric linear GCD curves of CNT@STO films at 5 mA·cm⁻², originating from hybrid capacitance performance combined with DLC and pseudocapacitance. Because a large IR drop is observed in GCD plots, it suggests that capacitance values should be calculated based on the CV plots. Herein, the areal capacitance (C_s) of different CNT@STO and standard CNT calculated from 5, 10, 30, 50, and 100 mV·s⁻¹ are shown in Figure 6c based on the area of the whole composite. It turns out that the CNT@STO-25 electrode exhibits the maximum C_s value, which is 3949 mF·cm⁻² at 5 mV·s⁻¹. To explore the kinetic processes of energy storage, the AC impedance technique (EIS) test was performed on these samples, as shown in Figure 6d. Due to the hybrid capacitance performance, the Nyquist curves comprise Warburg semicircles and straight lines at high- and low-frequency ranges, respectively. The inset of this figure displays the corresponding equivalent circuit diagram, and the electrical elements are as follows: such as solution resistance (R_s), constant phase element, charge-transfer resistance between solution and electrode (R_{ct}), pseudocapacitance (C_p), and Warburg impedance (W_o). Because all electrochemical tests have been conducted in the same solution, the R_s values of different samples are all around 1.3 Ω. Meanwhile, the R_{ct} values of CNT, CNT@STO-15, CNT@STO-20, CNT@STO-25, and CNT@STO-30 are 0.1, 0.1, 0.11, 0.15, and 0.17 Ω, respectively. These results confirm that STO, as semiconductors, do not reduce the conductivity characteristics of CNT excessively when compounded with it. Because of their good conductivity and fast transfer kinetics, these CNT@STO films all possess superior energy storage performance.

Normally, the more STO is added, the better the C_s value of the composite film should be improved, and the results of CNT@STO-15, CNT@STO-20, and CNT@STO-25 are well in line with this inference. However, a higher STO content has not brought superior performance to the CNT@STO-30 electrode, which can be attributed to excessive grain growth, resulting in a decrease in surface active sites and a reduction of ion intercalation within the lattice. Owing to these two factors, interface bonding properties between STO and CNT surfaces declined, leading to a loss of ionic and charge transmission pathways. In addition, the doubled grain size and crystallization behavior of nonperovskite phase also reduce the storage sites for anions in STO. Therefore, we can conclude that the electrochemical properties of CNT@STO films are not always better with increasing amounts of STO. In particular, the C_s values of CNT@STO electrodes are not improved at high current density, which may be caused by an

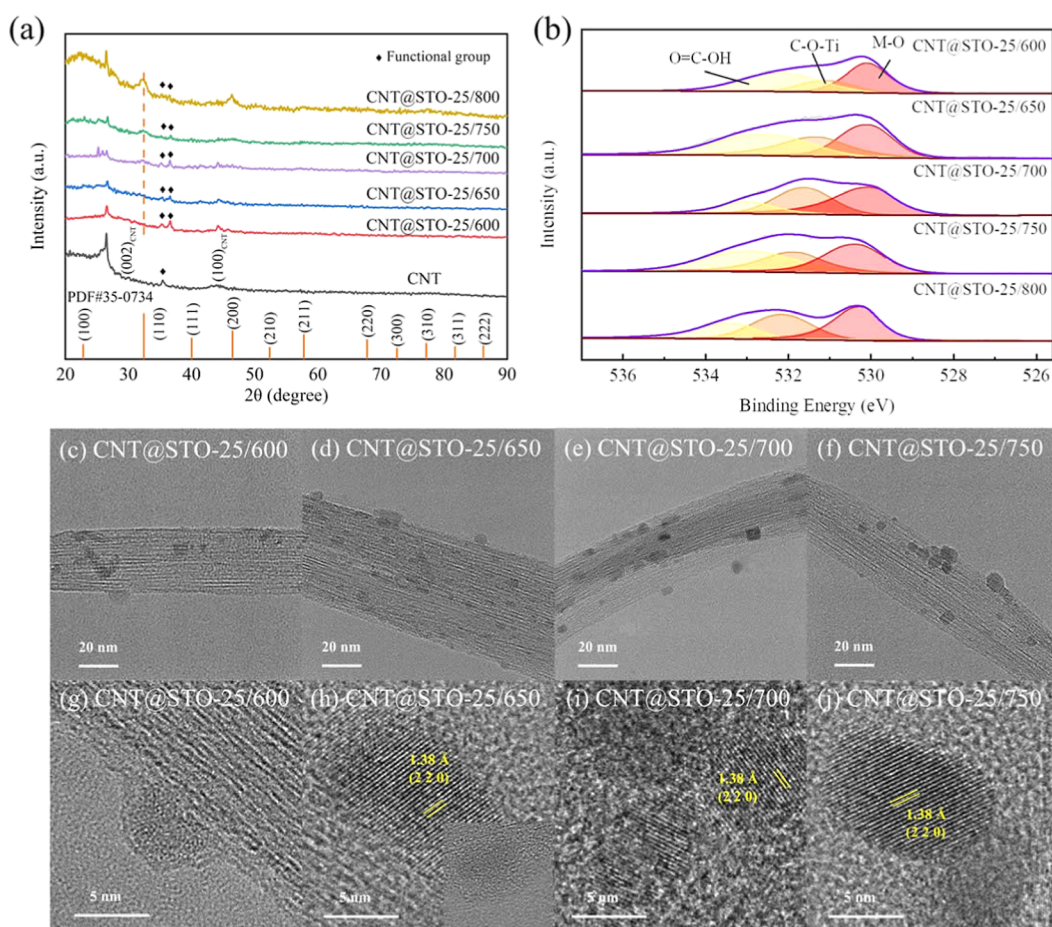


Figure 7. Characterization diagram of CNT@STO-25 films at different sintering temperatures. (a) XRD. (b) XPS of O 1s. (c–f) TEM. (g–j) HRTEM.

insufficient rate of ion transfer between interfaces. As the OH[−] adsorbed on the surface of the CNT is transferred via C–O–M bonds, the capacitance contributed by the oxygen intercalation mechanism is limited at high current density (Figure 6e).

In general, although raising the STO content is advantageous for improving the contribution of the pseudocapacitance in the CNT@STO composite film, a high degree of STO can lead to grain growth and an increase in foreign phases, thus affecting charge storage and transfer. As comprehensively analyzed, the CNT@STO-25 sample shows the optimum compound ratio.

3.2. Influence of Heat-Treatment Temperature. The above study suggests that electrochemical performance can be impacted by the grain size of STO. However, the size and distribution of STO are often determined with their calcination process. In view of this, we further investigate the influence of thermal treatment temperature variation on the charge storage properties of the CNT@STO-25 film. In this regard, we synthesized different CNT@STO-25 films at 600, 650, 700, and 750 °C for comparison with the previously prepared at 800 °C. For convenience, this article records these samples as CNT@STO-25/600, CNT@STO-25/650, CNT@STO-25/700, CNT@STO-25/750, and CNT@STO-25/800, respectively. As the electrochemical properties of perovskite type oxides in the crystalline state are much superior to those in the amorphous state, it is particularly valuable to identify the calcination temperature of full lattice formation.

The XRD spectrogram of these CNT@STO-25 samples synthesized at different temperatures, as shown in Figure 7a, exhibits no obvious characteristic peak outside of the CNT peaks at 600 °C, indicating an amorphous structure of STO. When the processing temperature is increased to 650 °C, there is a weak peak belonging to the (110) plane of cubic crystal system. As a result of that, we estimate that partial STO has already formed crystal nuclei. At 700 °C, a broad peak replaces the previous weak one, suggesting that STO grains have grown to a fully crystalline state. Besides, for the CNT@STO-25/750 and CNT@STO-25/800, a rise in peak intensity indicates the development of STO grain is correlated positively with calcination temperature.

To improve the charge storage performance of CNT@STO-25, it is important to promote charge-transfer efficiency at the interface in addition to lattice integrity. Herein, the XPS depth profiling and peak decomposition techniques were used to study these CNT@STO-25 films with various temperatures. As present in Figure 7b, the O 1s characteristic peaks corresponding to CNT@STO-25/600, CNT@STO-25/650, CNT@STO-25/700, and CNT@STO-25/750 all perform two adjacent spin–orbit peaks at the binding energies of 532.5 and 530.3 eV, belonging to C–O and M–O bonds, respectively, like the one at 800 °C before. After fitting, all spin–orbit peaks of C–O bonds can be divided into two peaks corresponding to the carboxyl groups and C–O–M bonds, respectively, which are consistent with previous results. Moreover, the investigations note that the C–O–M bonds and M–O bonds have

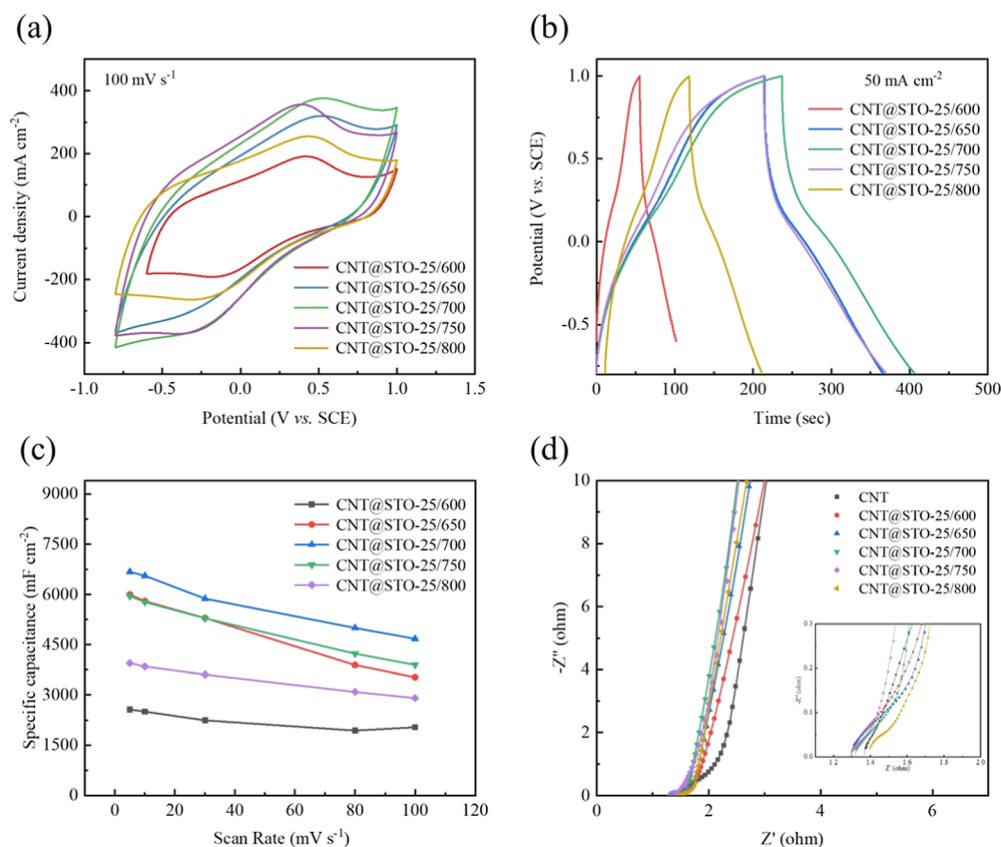


Figure 8. Electrochemical testing of CNT and CNT@STO-25 films at different synthesis temperatures, (a) CV at 100 mV s^{-1} . (b) GCD at 50 mA cm^{-2} . (c) Areal capacitance. (d) Nyquist plots.

relatively low content, while the sintering temperature is below $700 \text{ }^\circ\text{C}$, which may lead to a diminution of interfacial interaction. However, owing to the very close intensity and location of the characteristic peaks at 700 , 750 , and $800 \text{ }^\circ\text{C}$, these films should have similar interface properties. Based on these findings, $700 \text{ }^\circ\text{C}$ may probably be an optimal temperature.

Although the SEM characterization (Figure S4) of these CNT@STO-25 films all exhibited a similar microcosmic appearance, we still investigated the micro variations of these CNT@STO-25 samples at different temperatures by using the TEM and HRTEM characterization. From Figure 7c–f, it is observed that all nanoparticles possess a size of $5\text{--}10 \text{ nm}$ and tightly pack on the CNT surface. Naturally, there are larger grains at higher temperatures. The drawing of HRTEM are shown in Figure 7g–j, indicating the information on their lattice structure. Certainly, no recognizable lattice stripes in the CNT@STO-25/600 sample confirm its amorphous form. However, the corresponding lattice fringes of the (220) plane can already be identified in a few of the STO particles in the CNT@STO-25/650 sample, determining the presence of nuclei. For the CNT@STO-25 films prepared above $700 \text{ }^\circ\text{C}$, their lattice fringes are clearly visible, and interplane spacing remains unchanged. Therefore, in this work, $700 \text{ }^\circ\text{C}$ should be selected.

In order to prove it, the electrochemical performances of CNT@STO-25 films prepared at 600 , 650 , 700 , and $750 \text{ }^\circ\text{C}$ were evaluated by CV and GCD measurements, and the corresponding results are drawn in Figures S5 and S6. As shown in Figure 8a, the CV curves of CNT@STO-25/600 only have a narrow voltage window of 1.6 V due to the

amorphous state of STO. In contrast, the other CNT@STO-25 films all display a similar deformed rectangle shape, and the positions of the redox peaks also stay constant. Furthermore, Figure 8b exhibits different GCD curves for these CNT@STO-25 films. Their shapes are all asymmetric, apparently containing pseudocapacitor behavior. From the C_s value curves presented in Figure 8c, we can confirm that $700 \text{ }^\circ\text{C}$ is the optimized reaction temperature for the synthesis of the composites. According to the results, the CNT@STO-25 film prepared at $600 \text{ }^\circ\text{C}$ shows an apparent low C_s due to an incomplete formation of STO crystal, while the enhancement in the processing temperature can improve their energy storage performance. However, with temperatures over $700 \text{ }^\circ\text{C}$, the C_s drops because the increased lattice perfection of the STO on the CNTs reduces the number of channels for the ion diffusion and thus weakens the electrochemical properties. Hence, in this study, the maximum C_s value of the CNT@STO-25 electrode is $6682 \text{ mF}\cdot\text{cm}^{-2}$, which is achieved at a scan rate of $5 \text{ mV}\cdot\text{s}^{-1}$. Although CNT@STO-25/650 and CNT@STO-25/750 all share a relatively close C_s at $5 \text{ mV}\cdot\text{s}^{-1}$, their energy storage performance decreases rapidly with an increasing scan rate. As a result, the CNT@STO-25/700 sample displays better rate capability than the others. Additionally, the influences of the synthesis temperature on their performance can also be proven from the EIS results (Figure 8d). For these samples synthesized below $700 \text{ }^\circ\text{C}$, their R_{ct} values increase to about $0.25 \text{ } \Omega$, indicating an insufficient interface bonding strength owing to their incomplete reaction. With an increased sintering temperature, the R_{ct} values return back to around $0.14 \text{ } \Omega$, which can be attributed to the completed formation of

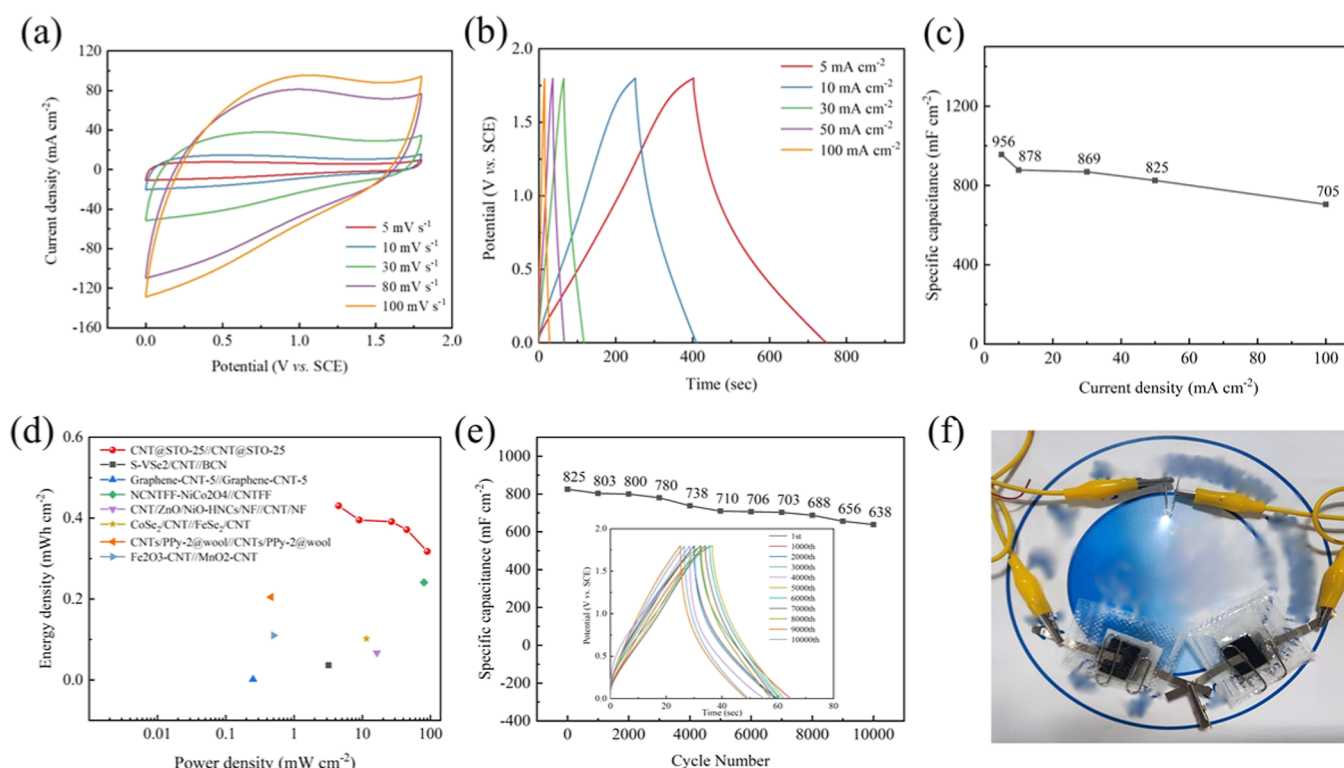


Figure 9. (a) CV curves of CNT@STO-25//CNT@STO-25 device at different scan rates. (b) GCD curves of CNT@STO-25//CNT@STO-25 device at different current densities. (c) Comparison of the areal capacitance as a function of current density for CNT@STO-25//CNT@STO-25 device. (d) Ragone plots for the CNT@STO-25//CNT@STO-25 supercapacitor in comparison with references. (e) Cycling performance of the CNT@STO-25//CNT@STO-25 device at 50 mA cm⁻². (f) White LED illuminated by CNT@STO-25//CNT@STO-25 devices.

Table 1. Areal Energy Density (E) and Areal Power Density (P) of Flexible Supercapacitor Devices Reported Before

sample	$E/\mu\text{W h}\cdot\text{cm}^{-2}$	$P/\text{mW}\cdot\text{cm}^{-2}$	references
CNTs/PPy-2@wool//CNTs/PPy-2@wool	204.8	0.46	44
graphene-CNT-5//graphene-CNT-5	1.36	0.25	45
S-VSe ₂ /CNT//BCN	36.3	3.2	46
NCNTFF-NiCo ₂ O ₄ //CNTFF	241	80.2	47
CoSe ₂ /CNT//FeSe ₂ /CNT	102	11.42	48
CNT/ZnO/NiO-HNCs/NF//CNT/NF	67	16.25	49
Fe ₂ O ₃ -CNT//MnO ₂ -CNT	110	0.5	50
CNT@STO-25//CNT@STO-25	430.2	4.5	this work

STO. In summary, to derive better performing CNT@STO-25 films, we prefer to process them at 700 °C.

3.3. Performance of Flexible Device. In this work, as the CNT@STO-25 electrode features a large voltage window, it is possible to achieve a better energy storage performance by assembling a symmetrical flexible supercapacitor. This device was denoted as CNT@STO-25//CNT@STO-25, and its electrochemical performance was examined through using a two-electrodes system. Figure 9a shows its CV curves at a scan rate of 5–100 mV s⁻¹. These rectangular shapes with similar forms can be easily observed, indicating its good rate capability. Meanwhile, its GCD curves tested at different current densities of 5–100 mA·cm⁻² are presented in Figure 9b. As all curves have similar asymmetric shapes, this device should have an excellent Coulomb efficiency. These results also confirm its 1.8 V operating voltage, suggesting a high utility for the electrodes.

In Figure 9c, the C_s values of CNT@STO-25//CNT@STO-25 device calculated from the corresponding GCD curves are 956, 878, 869, 825, and 705 mF·cm⁻² (703, 645, 638, 606, and

518 F·g⁻¹), showing a 73.7% retention of its original value after a 20 times increase in current density. As a hybrid electrode, its considerable rate performance may be ascribed to the contribution of the EDLC provided from CNTs. Moreover, this excellent rate performance also indicates that chemical bonding is advantageous for facilitating better interface synergistic effects between the two components. For supercapacitors, energy density (E) and power density (P) are both important indices for judging energy storage performance, and thus the corresponding values calculated by eqs 2 and 3 are exhibited in Figure 9d. Herein, the maximum E of the device, based on the area of the whole composite, is 430.2 $\mu\text{W h}\cdot\text{cm}^{-2}$ with a P of 4.5 mW·cm⁻², while the E still remains at about 317.25 $\mu\text{W h}\cdot\text{cm}^{-2}$, which is achieved at a higher P of 90 mW·cm⁻². Meanwhile, their corresponding E and P based on the film mass are exhibited in Figure S7. In addition, various E and P values of several supercapacitor devices fabricated by using different modified CNT electrodes are also displayed in this figure for comparison (Table 1). Due to its higher energy density achieved at the same power density, the CNT@STO-

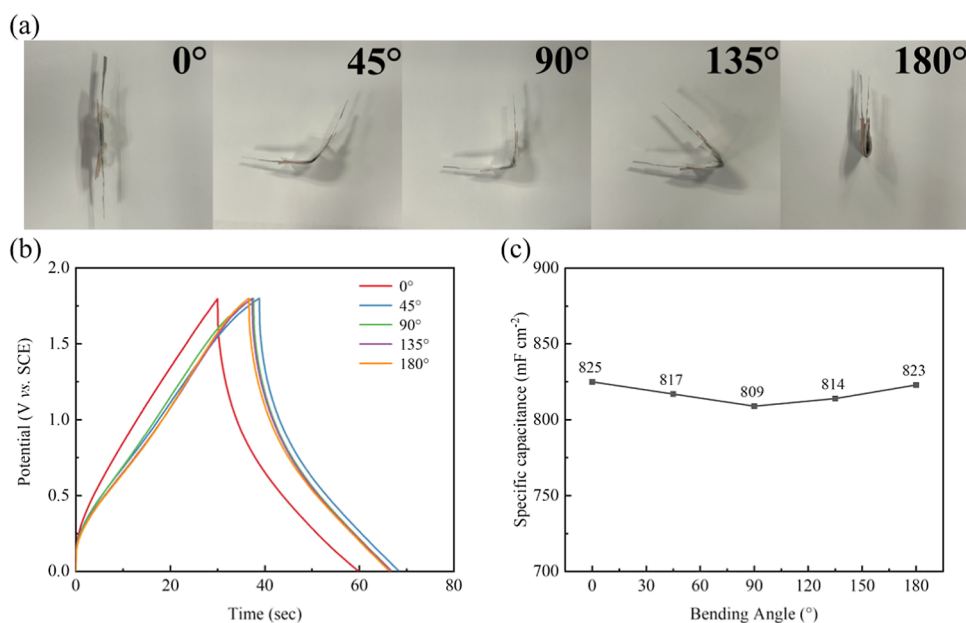


Figure 10. (a) Digital photographs of the CNT@STO-25//CNT@STO-25 device bent at different angles (0, 45, 90, 135, and 180°). (b) GCD curves of CNT@STO-25//CNT@STO-25 device bent at different angles. (c) Areal capacitance of CNT@STO-25//CNT@STO-25 device obtained at each angle (0, 45, 90, 135, and 180°).

25//CNT@STO-25 device can be considered as an outstanding potential supercapacitor for wearable devices.

Normally, one essential issue for high-performance supercapacitor devices in applications is the cyclic stability. To explore its long-term cycling performance, we conducted a 10,000 times charge–discharge cyclic test at 50 mA·cm⁻². As shown in Figure 9e, after the first 2000 cycles, the performance of the device drops a little and remains above 95%. However, its C_s decrease gradually in the following cycles and stays at about 706 mF cm⁻² after 7000 cycles, which retains nearly 85% of its initial value. In the last 2000 cycles, its C_s declines rapidly, with a final retention rate of only 77.3%. According to the preceding analysis, during the charge/discharge process, anions insert into the STO lattice layer from the CNT surface by interfacial transfer, accompanied by in situ redox reactions of Ti. Generally, the Ti ions in the Ti–O–C bonds at the interface are the most active, which may impair the interface strength because of its self-reaction in cycle and thus lead to a deficiency of cyclic stability. Nevertheless, the results demonstrate that its cyclic stability is still appreciable. Besides, we have verified its practical applicability by using two devices in series to light up LED lights. From the digital photo of Figure 9f, it is observed the devices can be served as a source to power a white LED.

In actual application scenarios, the flexible devices not only require high energy storage performance but also demand good mechanical flexibility. To investigate mechanical stability, we bent the device to different angles, including 0, 45, 90, 135, and 180°, and studied the change in its electrochemical properties. The views after bending, different GCD curves, and C_s values corresponding to the different bending angles are shown in Figure 10a–c, respectively. These GCD curves, tested at 50 mA·cm⁻², all present similar shapes with negligible changes. Meanwhile, the C_s values also confirm that its performance can retain over 98% of the unbent one at any bending angle. The achievement of a minimum value at 90° can be attributed to the expansion of the gap between positive

and negative electrodes owing to folds in the device case. Thus, these results indicate its excellent mechanical stability and superior flexibility.

4. CONCLUSIONS

In this study, we successfully synthesized various CNT@STO composite films using a facile heat-reaction under an Ar atmosphere between STO precursors and CNTs. The results suggested that perovskite-type STO nanoparticles were tightly attached onto the CNT surface. Owing to the strong interface interaction from the formation of Ti–O–C bonds, the CNT@STO film showed superior conductivity and excellent energy storage performance. After varying different synthesis conditions, it was found that the composite prepared with a mass ratio of 25:75 for the STO vs CNTs and a calcination temperature of 700 °C possessed the highest areal capacitance of 6682 mF·cm⁻². The optimized CNT@STO-25 film used as electrodes for a flexible supercapacitor achieved an outstanding energy density of 430.2 μW h cm⁻² at a power density of 4.5 mW cm⁻². Furthermore, the device also displayed excellent mechanical stability, and its capacitance retention was over 98% after bending. Thus, it was proved that in situ preparation of MOs on the surface of carbon materials is an effective way to construct strong and beneficial interactions between the MOs and carbon materials. The CNT@STO composite is a good candidate for future applications.

■ ASSOCIATED CONTENT

Supporting Information

The Supporting Information is available free of charge at <https://pubs.acs.org/doi/10.1021/acsomega.4c01890>.

Calculation of the proportion of STO, I_D/I_G values of the CNT@STO composite membrane, TG curves of CNT and CNT@STO composites, CV curves of CNT and different CNT@STO electrodes at different scan rates, GCD curves of CNT and different CNT@STO electrodes at different current densities, SEM of CNT

and CNT@STO-25 films at different sintering temperatures, CV curves of CNT and CNT@STO-25 films at different sintering temperatures at different scan rates, GCD curves of CNT and CNT@STO-25 films at different sintering temperatures at different current densities, and Ragone plots for CNT@STO-25//CNT@STO-25 supercapacitor based on the film mass (PDF)

AUTHOR INFORMATION

Corresponding Authors

Yi Cao – Hubei Key Laboratory of Photoelectric Materials and Devices, School of Materials Science and Engineering, Hubei Normal University, Huangshi 435002, China; National Laboratory of Solid State Microstructures, Nanjing University, Nanjing 210093, China; Email: caoyi@hbnu.edu.cn

Wenfeng Qiu – South China Advanced Institute for Soft Matter Science and Technology, School of Emergent Soft Matter, South China University of Technology, Guangzhou 510640, China; Guangdong Provincial Key Laboratory of Functional and Intelligent Hybrid Materials and Devices, South China University of Technology, Guangzhou 510640, China; orcid.org/0000-0002-4935-3267; Email: wfqiu@scut.edu.cn

Authors

Yue Cao – South China Advanced Institute for Soft Matter Science and Technology, School of Emergent Soft Matter, South China University of Technology, Guangzhou 510640, China; Guangdong Provincial Key Laboratory of Functional and Intelligent Hybrid Materials and Devices, South China University of Technology, Guangzhou 510640, China

Shijingmin Li – South China Advanced Institute for Soft Matter Science and Technology, School of Emergent Soft Matter, South China University of Technology, Guangzhou 510640, China; Guangdong Provincial Key Laboratory of Functional and Intelligent Hybrid Materials and Devices, South China University of Technology, Guangzhou 510640, China

Jinhua Zhong – HXF SAW CO. LTD, Metallurgical Geology Bureau, Yichang 443005, China

Complete contact information is available at:
<https://pubs.acs.org/10.1021/acsomega.4c01890>

Notes

The authors declare no competing financial interest.

ACKNOWLEDGMENTS

Y.C., S.L., and W.Q. are thankful for the School of Emergent Soft Matter and the Guangdong Provincial Key Laboratory of Functional and Intelligent Hybrid Materials and Devices. J.Z. is thankful for the HXF SAW CO. Ltd. Y.C. is thankful for the Hubei Key Laboratory of Photoelectric Materials and Devices and the School of Materials Science and Engineering and the National Laboratory of Solid State Microstructures. Y.C. further acknowledges the support from the Natural Science Foundation of Hubei Province grant (grant numbers 2023AFD028 and 2023AFC035) and open project of National Laboratory of Solid State Microstructures (grant numbers M36003).

REFERENCES

- (1) Tan, K. M.; Babu, T. S.; Ramachandaramurthy, V. K.; Kasinathan, P.; Solanki, S. G.; Raveendran, S. K. Empowering smart grid: A comprehensive review of energy storage technology and application with renewable energy integration. *J. Energy Storage* **2021**, *39*, 102591.
- (2) Gan, Z.; Yin, J.; Xu, X.; Cheng, Y.; Yu, T. Nanostructure and Advanced Energy Storage: Elaborate Material Designs Lead to High-Rate Pseudocapacitive Ion Storage. *ACS Nano* **2022**, *16*, 5131–5152.
- (3) Almtiri, M.; Dowell, T. J.; Giri, H.; Wipf, D. O.; Scott, C. N. Electrochemically Stable Carbazole-Derived Polyaniline for Pseudocapacitors. *ACS Appl. Polym. Mater.* **2022**, *4*, 3088–3097.
- (4) Zhang, D.; Tan, C.; Zhang, W.; Pan, W.; Wang, Q.; Li, L. Expanded Graphite-Based Materials for Supercapacitors: A Review. *Molecules* **2022**, *27*, 716.
- (5) Niaz, N. A.; Shakoor, A.; Imran, M.; Khalid, N. R.; Hussain, F.; Kanwal, H.; Maqsood, M.; Afzal, S. Enhanced electrochemical performance of MoS₂/PPy nanocomposite as electrodes material for supercapacitor applications. *J. Mater. Sci. Mater. Electron.* **2020**, *31*, 11336–11344.
- (6) Yang, X.; Tian, Y.; Wu, B.; Jia, W.; Hou, C.; Zhang, Q.; Li, Y.; Wang, H. High-Performance Ionic Thermoelectric Supercapacitor for Integrated Energy Conversion-Storage. *Energy Environ. Mater.* **2022**, *5*, 954–961.
- (7) Zhang, G.; Hu, J.; Nie, Y.; Zhao, Y.; Wang, L.; Li, Y.; Liu, H.; Tang, L.; Zhang, X.; Li, D.; Sun, L.; Duan, H. Integrating Flexible Ultralight 3D Ni Micromesh Current Collector with NiCo Bimetallic Hydroxide for Smart Hybrid Supercapacitors. *Adv. Funct. Mater.* **2021**, *31*, 2100290.
- (8) Zhao, Z.; Xia, K.; Hou, Y.; Zhang, Q.; Ye, Z.; Lu, J. Designing flexible, smart and self-sustainable supercapacitors for portable/wearable electronics: from conductive polymers. *Chem. Soc. Rev.* **2021**, *50*, 12702–12743.
- (9) Zhang, Y.; Mei, H.; Cao, Y.; Yan, X.; Yan, J.; Gao, H.; Luo, H.; Wang, S.; Jia, X.; Kachalova, L.; Yang, J.; Xue, S.; Zhou, C.; Wang, L.; Gui, Y. Recent advances and challenges of electrode materials for flexible supercapacitors. *Coord. Chem. Rev.* **2021**, *438*, 213910.
- (10) Xiao, L.; Qi, H.; Qu, K.; Shi, C.; Cheng, Y.; Sun, Z.; Yuan, B.; Huang, Z.; Pan, D.; Guo, Z. Layer-by-layer assembled free-standing and flexible nanocellulose/porous Co₃O₄ polyhedron hybrid film as supercapacitor electrodes. *Adv. Compos. Hybrid Mater.* **2021**, *4*, 306–316.
- (11) Wang, Q.; Yang, Y.; Chen, W.; Zhang, C.; Rong, K.; Gao, X.; Fan, W. Reliable coaxial wet spinning strategy to fabricate flexible MnO₂-based fiber supercapacitors. *J. Alloys Compd.* **2023**, *935*, 168110.
- (12) Liu, H.; Xu, T.; Liang, Q.; Zhao, Q.; Zhao, D.; Si, C. Compressible cellulose nanofibrils/reduced graphene oxide composite carbon aerogel for solid-state supercapacitor. *Adv. Compos. Hybrid Mater.* **2022**, *5*, 1168–1179.
- (13) Swain, N.; Tripathy, A.; Thirumurugan, A.; Saravanakumar, B.; Schmidt-Mende, L.; Ramadoss, A. A brief review on stretchable, compressible, and deformable supercapacitor for smart devices. *Chem. Eng. J.* **2022**, *446*, 136876.
- (14) Luo, X.; Zheng, H.; Lai, W.; Yuan, P.; Li, S.; Li, D.; Chen, Y. Defect Engineering of Carbons for Energy Conversion and Storage Applications. *Energy Environ. Mater.* **2023**, *6*, No. e12402.
- (15) Xie, P.; Yuan, W.; Liu, X.; Peng, Y.; Yin, Y.; Li, Y.; Wu, Z. Advanced carbon nanomaterials for state-of-the-art flexible supercapacitors. *Energy Storage Mater.* **2021**, *36*, 56–76.
- (16) Wang, T.; Liu, Z.; Li, P.; Wei, H.; Wei, K.; Chen, X. Lignin-derived carbon aerogels with high surface area for supercapacitor applications. *Chem. Eng. J.* **2023**, *466*, 143118.
- (17) Liu, X.; Lu, Z.; Pan, H.; Cheng, J.; Dou, J.; Huang, X.; Chen, X. Investigation of functionalization effect of carbon nanotubes as supercapacitor electrode material on hydrogen evolution side-reaction by scanning electrochemical microscopy. *Electrochim. Acta* **2022**, *429*, 141056.

- (18) Jiang, H.; Zhang, Y.; Sheng, F.; Li, W.; Li, J.; Huang, D.; Guo, P.; Wang, Y.; Zhu, H. Graphene Film with a Controllable Microstructure for Efficient Electrochemical Energy Storage. *ACS Appl. Mater. Interfaces* **2023**, *15*, 13086–13096.
- (19) Yang, H. C.; Chen, Y. Y.; Suen, S. Y.; Lee, R. H. Triazine-based covalent organic framework/carbon nanotube fiber nanocomposites for high-performance supercapacitor electrodes. *Polymer* **2023**, *273*, 125853.
- (20) Turchi Moghadam, M. T.; Seifi, M.; Jamali, F.; Azizi, S.; Askari, M. B. ZnWO₄-CNT as a superior electrode material for ultra-high capacitance supercapacitor. *Surface. Interfac.* **2022**, *32*, 102134.
- (21) Lee, S.; An, G.-H. Interface Engineering of Carbon Fiber-Based Electrode for Wearable Energy Storage Devices. *Adv. Fiber Mater.* **2023**, *5*, 1749–1758.
- (22) Tong, B.; Wei, W.; Wu, Z.; Zhao, L.; Ye, W.; Wang, J.; Chen, W.; Soutis, C.; Mi, L. Interface Engineering Based on Multinanoscale Heterojunctions between NiO Quantum Dots, N-Doped Amorphous Carbon and Ni for Advanced Supercapacitor. *ACS Appl. Energy Mater.* **2021**, *4*, 3221–3230.
- (23) Kariper, I. A.; Korkmaz, S.; Karaman, C.; Karaman, O. High energy supercapacitors based on functionalized carbon nanotubes: Effect of atomic oxygen doping via various radiation sources. *Fuel* **2022**, *324*, 124497.
- (24) Prakash, D.; Manivannan, S. N. B co-doped and Crumpled Graphene Oxide Pseudocapacitive Electrode for High Energy Supercapacitor. *Surface. Interfac.* **2021**, *23*, 101025.
- (25) Wang, B. Q.; Gong, S. H.; Sun, Q. S.; Liu, F.; Wang, X. C.; Cheng, J. P. Carbon nanotubes refined mesoporous NiCoO₂ nanoparticles for high-performance supercapacitors. *Electrochim. Acta* **2022**, *402*, 139575.
- (26) Jyothibasu, J. P.; Wang, R. H.; Ong, K.; Ong, J. H. L.; Lee, R. H. Scalable synthesis of γ -Fe₂O₃-based composite films as freestanding negative electrodes with ultra-high areal capacitances for high-performance asymmetric supercapacitors. *Cellulose* **2022**, *29*, 321–340.
- (27) Mefford, J. T.; Hardin, W. G.; Dai, S.; Johnston, K. P.; Stevenson, K. J. Anion charge storage through oxygen intercalation in LaMnO₃ perovskite pseudocapacitor electrodes. *Nat. Mater.* **2014**, *13*, 726–732.
- (28) Xiong, X. H.; Yang, L. T.; Liang, G. S.; Liu, Z. W.; Yang, Z. Q.; Zhang, R. X.; Wang, C.; Che, R. C. Cation-Vacancy Ordered Superstructure Enhanced Cycling Stability in Tungsten Bronze Anode. *Adv. Energy Mater.* **2022**, *12*, 2201967.
- (29) Liu, Y.; Wang, Z. B.; Zhong, Y. J.; Xu, X. M.; Veder, J. P. M.; Rowles, M. R.; Saunders, M.; Ran, R.; Shao, Z. P. Activation-free supercapacitor electrode based on surface-modified Sr₂CoMo_{1-x}Ni_xO_{6- δ} perovskite. *Chem. Eng. J.* **2020**, *390*, 124645.
- (30) Tanapongpisit, N.; Wongprasod, S.; Laohana, P.; Kim, S.; Butburee, T.; Meevasana, W.; Maensiri, S.; Bark, C. W.; Saenrang, W. Effects of the particle size of BaMnO₃ powders on the electrochemical performance of supercapacitor electrodes. *Mater. Lett.* **2022**, *319*, 132258.
- (31) Qiao, Y.; Liu, G.; Xu, R.; Hu, R.; Liu, L.; Jiang, G.; Demir, M.; Ma, P. SrFe_{1-x}Zr_xO_{3- δ} perovskite oxides as negative electrodes for supercapacitors. *Electrochim. Acta* **2023**, *437*, 141527.
- (32) Nan, H.; Hu, X.; Tian, H. Recent advances in perovskite oxides for anion-intercalation supercapacitor: A review. *Mater. Sci. Semicond. Process.* **2019**, *94*, 35–50.
- (33) Yang, L. T.; Xiong, X. H.; Liang, G. S.; Li, X.; Wang, C.; You, W. B.; Zhao, X. B.; Liu, X. H.; Che, R. C. Atomic Short-Range Order in a Cation-Deficient Perovskite Anode for Fast-Charging and Long-Life Lithium-Ion Batteries. *Adv. Mater.* **2022**, *34*, 2200914.
- (34) Shafi, P. M.; Ganesh, V.; Bose, A. C. LaMnO₃/RGO/PANI Ternary Nanocomposites for Supercapacitor Electrode Application and Their Outstanding Performance in All-Solid-State Asymmetrical Device Design. *ACS Appl. Energy Mater.* **2018**, *1*, 2802–2812.
- (35) Harputlu, E. Nanoarchitectonics of the supercapacitor performance of LaNiO₃ perovskite on the graphitic-C₃N₄ doped reduced graphene oxide hydrogel. *Colloids Surf., A* **2022**, *632*, 127787.
- (36) Li, J. Y.; Luo, W. T.; Wang, X. Q.; Yu, C.; Zhang, Y. J.; Meng, F. B. Preparation and research of high-performance LaFeO₃/RGO supercapacitor. *J. Solid State Electrochem.* **2022**, *26*, 1291–1301.
- (37) Garces, L.; Oliva, J.; Padmasree, K. P.; Mtz-Enriquez, A. I.; Rodriguez-Gonzalez, V. Ca_{2.9}La_{0.1}Co₄O₉/graphene composite electrodes for improved electrochemical performance of cellulose-based supercapacitors. *Mater. Chem. Phys.* **2023**, *301*, 127612.
- (38) Gopi, U. V.; Bhojane, P.; Smaran, K. S. Engineering oxygen-deficient nanocomposite comprising LaNiO_{3- δ} and reduced graphene oxide for high-performance pseudocapacitors. *J. Energy Storage* **2022**, *54*, 105301.
- (39) Zhu, Z.; Cui, C.; Bai, Y.; Gao, J.; Jiang, Y.; Li, B.; Wang, Y.; Zhang, Q.; Qian, W.; Wei, F. Advances in Precise Structure Control and Assembly toward the Carbon Nanotube Industry. *Adv. Funct. Mater.* **2022**, *32*, 2109401.
- (40) Liu, Y.; Chen, X.; Lin, H.; Zhou, P.; Ying, Y. A self-supporting P-doped CNT@MnCo₂O₄/Co₃O₄ electrode with ion and electron-conductive hierarchical structure for high performance supercapacitor. *J. Alloys Compd.* **2023**, *958*, 170453.
- (41) Wei, X.; Zhou, X.; Li, L.; Feng, W.; Wu, H. Rational designing carbon nanotubes incorporated oxygen vacancy-enriched bimetallic (Ni, Co) oxide nanocages for high-performance hybrid supercapacitor. *Appl. Surf. Sci.* **2023**, *613*, 155959.
- (42) Li, S. L.; Zhang, M. D.; Feng, Z. X.; Huang, Y. C.; Qian, T.; Hu, H.; Zheng, X.; Liu, P. F.; Liu, H. Y.; Xing, T.; Wu, M. B. Anchoring perovskite-Type FeMnO₃ microspheres on CNT conductive networks via electrostatic self-assembly for high-performance lithium-ion capacitors. *Chem. Eng. J.* **2021**, *424*, 130315.
- (43) Xue, Y.; Ruan, P.; Zhu, L.; Cao, Y.; Fu, W.; Huang, J.; Qiu, W. Flexible Hf₆Ta₂O₁₇@ acidified carbon nanotube composite films with enhanced interfacial interaction for high-performance supercapacitors. *Ceram. Int.* **2023**, *49*, 22089–22099.
- (44) Wu, Z.; Zhang, X.; Yang, P.; Yang, J.; Liu, Y.; Zhang, T.; Lu, M. Di-oxidant sandwich-type polymerization strategy of polypyrrole on CNTs@wool felt for supercapacitors. *Electrochim. Acta* **2021**, *392*, 139056.
- (45) Wang, Y.; Zhang, Y.; Wang, G.; Shi, X.; Qiao, Y.; Liu, J.; Liu, H.; Ganesh, A.; Li, L. Direct Graphene-Carbon Nanotube Composite Ink Writing All-Solid-State Flexible Microsupercapacitors with High Areal Energy Density. *Adv. Funct. Mater.* **2020**, *30*, 1907284.
- (46) Raj, K. A. S.; Pramoda, K.; Rout, C. S. Assembling a high-performance asymmetric supercapacitor based on pseudocapacitive S-doped VSe₂/CNT hybrid and 2D borocarbonitride nanosheets. *J. Mater. Chem. C* **2023**, *11*, 2565–2573.
- (47) Liang, Y.; Luo, X.; Zhang, Y.; Yang, L.; Hu, Z.; Zhu, M. Nickel cobaltite nanowire arrays grown on nitrogen-doped carbon nanotube fiber fabric for high-performance flexible supercapacitors. *J. Colloid Interface Sci.* **2023**, *645*, 391–399.
- (48) Wang, Q.; Ran, X.; Shao, W.; Miao, M.; Zhang, D. High performance flexible supercapacitor based on metal-organic-framework derived CoSe₂ nanosheets on carbon nanotube film. *J. Power Sources* **2021**, *490*, 229517.
- (49) Jayababu, N.; Jo, S.; Kim, Y.; Kim, D. Preparation of NiO decorated CNT/ZnO core-shell hybrid nanocomposites with the aid of ultrasonication for enhancing the performance of hybrid supercapacitors. *Ultrason. Sonochem.* **2021**, *71*, 105374.
- (50) Wang, Y.; Xiao, J.; Zhang, T.; Ouyang, L.; Yuan, S. Single-Step Preparation of Ultrasmall Iron Oxide-Embedded Carbon Nanotubes on Carbon Cloth with Excellent Superhydrophilicity and Enhanced Supercapacitor Performance. *ACS Appl. Mater. Interfaces* **2021**, *13*, 45670–45678.